

ARMY RESEARCH LABORATORY



A Prediction of 94-GHz Radiometer Performance in Various Environmental Conditions for Army Applications

by David Wikner

ARL-TR-1103

September 1996

19961115 038

DTIC QUALITY INSPECTED 3

Approved for public release; distribution unlimited.

The findings in this report are not to be construed as an official Department of the Army position unless so designated by other authorized documents.

Citation of manufacturer's or trade names does not constitute an official endorsement or approval of the use thereof.

Destroy this report when it is no longer needed. Do not return it to the originator.

REPORT DOCUMENTATION PAGE			Form Approved OMB No. 0704-0188	
Public reporting burden for this collection of information is estimated to average 1 hour per response, including the time for reviewing instructions, searching existing data sources, gathering and maintaining the data needed, and completing and reviewing the collection of information. Send comments regarding this burden estimate or any other aspect of this collection of information, including suggestions for reducing this burden, to Washington Headquarters Services, Directorate for Information Operations and Reports, 1215 Jefferson Davis Highway, Suite 1204, Arlington, VA 22202-4302, and to the Office of Management and Budget, Paperwork Reduction Project (0704-0188), Washington, DC 20503.				
1. AGENCY USE ONLY (Leave blank)		2. REPORT DATE September 1996		3. REPORT TYPE AND DATES COVERED Final
4. TITLE AND SUBTITLE A Prediction of 94-GHz Radiometer Performance in Various Environmental Conditions for Army Applications			5. FUNDING NUMBERS DA PR: AH16 PE: 62120A	
6. AUTHOR(S) David Wikner				
7. PERFORMING ORGANIZATION NAME(S) AND ADDRESS(ES) U.S. Army Research Laboratory Attn: AMSRL-SE-RM 2800 Powder Mill Road Adelphi, MD 20783-1197			8. PERFORMING ORGANIZATION REPORT NUMBER ARL-TR-1103	
9. SPONSORING/MONITORING AGENCY NAME(S) AND ADDRESS(ES) U.S. Army Research Laboratory 2800 Powder Mill Road Adelphi, MD 20783-1197			10. SPONSORING/MONITORING AGENCY REPORT NUMBER	
11. SUPPLEMENTARY NOTES AMS code: 622120.H1611 ARL PR: 51E21B				
12a. DISTRIBUTION/AVAILABILITY STATEMENT Approved for public release; distribution unlimited.			12b. DISTRIBUTION CODE	
13. ABSTRACT (Maximum 200 words) <p>A prediction of 94-GHz imaging radiometer performance is made for three military scenarios in a variety of weather conditions. The scenarios considered are a ground-to-ground and an air-to-ground tank-sized target detection scenario and an aircraft landing-aid scenario. Simple models of atmospheric signal attenuation are used to calculate the scene temperature that would be present at a sensor with a 3- by 3-ft square antenna at ranges of 500 to 5000 m. This information is used to determine the range at which scene imaging or target detection is no longer possible. It is shown that, in scenarios where tank-sized targets are involved, spatial resolution usually limits system performance before most environmental conditions do. The only exception to this is in cases of moderate and heavy rain, where the signal attenuation is quite large. Given a sensor of sufficient temperature resolution, the landing-aid scenario is shown to be a reasonable scenario, especially in foggy conditions.</p>				
14. SUBJECT TERMS Radiometer, millimeter-wave			15. NUMBER OF PAGES 27	
			16. PRICE CODE	
17. SECURITY CLASSIFICATION OF REPORT Unclassified	18. SECURITY CLASSIFICATION OF THIS PAGE Unclassified	19. SECURITY CLASSIFICATION OF ABSTRACT Unclassified	20. LIMITATION OF ABSTRACT UL	

Contents

1. Introduction	5
2. MMW Radiometry Theory	6
3. Atmospheric Effects Theory	9
4. Results	10
4.1 <i>Armored Target Imaging</i>	10
4.2 <i>Landing System</i>	11
5. Discussion	18
6. Conclusion	22
Acknowledgments	22
References	22
Distribution	25

Figures

1. Calculated radiometer scene contrast, $\Delta T(K)$, for ground-to-ground scenario in clear air with various water vapor densities	13
2. Calculated radiometer scene contrast, $\Delta T(K)$, for ground-to-ground scenario through two fog visibilities	14
3. Calculated radiometer scene contrast, $\Delta T(K)$, for ground-to-ground scenario for two cloud cover types	14
4. Calculated radiometer scene contrast, $\Delta T(K)$, for ground-to-ground scenario in various rain rate conditions	15
5. Calculated radiometer scene contrast, $\Delta T(K)$, for air-to-ground scenario in clear air with various water vapor densities	16
6. Calculated radiometer scene contrast, $\Delta T(K)$, for air-to-ground scenario through two fog visibilities	16
7. Calculated radiometer scene contrast, $\Delta T(K)$, for air-to-ground scenario for two cloud cover types	17
8. Calculated radiometer scene contrast, $\Delta T(K)$, for air-to-ground scenario in various rain rate conditions	17
9. Calculated radiometer scene contrast, $\Delta T(K)$, for landing-aid scenario through two fog visibilities	18
10. Spatial resolution of 3- by 3-ft square antenna at 94 GHz	20

Tables

1. Noise cutoff ranges for ground-to-ground metal target scenario for various environmental conditions and temperature resolutions	19
2. Noise cutoff ranges for air-to-ground metal target scenario for various environmental conditions and temperature resolutions	19
3. Noise cutoff ranges for landing-aid scenario for various environmental conditions and temperature resolutions	19

1. Introduction

Passive millimeter-wave (MMW) sensors that use the latest developments in monolithic microwave integrated circuit (MMIC) technology and signal processing techniques are currently being developed for a variety of military and civilian applications [1–5]. Advances in W-band low-noise receivers, detectors, and processing methods have improved the possible performance of these sensors. As a result, theoretical predictions of potential system performance are required to support the development of these new sensor designs. This report supports the Army Research Laboratory's (ARL's) passive MMW imager program and presents a general approach to the prediction of passive MMW imager system performance in a variety of weather conditions.

Passive MMW sensors can be used when clouds, fog, or other atmospheric effects disrupt the imaging capabilities of other types of passive sensors such as forward-looking infrared (FLIR) and optical sensors. Passive MMW imagers, though, have a lower spatial resolution than these other sensors, and some types of weather will severely degrade a MMW imager's performance. The purpose of this report is to assess the performance of passive MMW sensors operating at about 94 GHz for a variety of atmospheric conditions and in a few scenarios that are of interest to the Army. The atmospheric conditions modeled are common weather scenarios and are meant to represent possible sensor operating conditions. All imager system parameters are left out of the analysis except for antenna size and center frequency. Included, however, is a description of the variation that occurs in system performance with various receiver noise figures so that the analysis can be applied to a variety of sensors.

Three imaging scenarios have been chosen for this study. The first is a ground-based sensor and an armored vehicle target. The second scenario represents an airborne sensor and an armored vehicle target, and the third represents an imager mounted on an aircraft that is landing on a concrete runway. Predicted image quality is assessed by calculating the scene temperature contrast that is present at the sensor antenna and comparing this to system temperature resolution.

This study is organized into the following sections:

MMW Radiometry Theory—basic equations describing passive MMW imaging phenomena.

Atmospheric Effects Theory—atmospheric models used to calculate MMW signal attenuation.

Results—details of scene temperature calculations and presentation of results.

Discussion—possible use of results for Army applications.

Conclusion—summary of results.

2. MMW Radiometry Theory

Typically, Earth-observing radiometers are used to image a scene composed of a wide variety of objects that naturally emit and reflect MMW radiation. The amount of radiation emitted by an object is proportional to its physical temperature. For the case of a black body, this radiation is described by the Rayleigh-Jeans approximation of Planck's law for black bodies. This equation, written in terms of thermal source brightness, is

$$B = \frac{2kT}{\lambda^2} , \quad (1)$$

where B is the thermal source brightness in units of watts/meters²/hertz/steradian, k is Boltzmann's constant in joules/Kelvin, T is the physical temperature of the source in Kelvin, and λ is the signal wavelength in meters. As equation (1) indicates, temperature is directly proportional to the thermal source brightness and thus the MMW power emitted by a black body source.

Most of the objects in a radiometer scene are not black bodies. That is, they have emissivities of less than one. So, to correctly calculate the power emitted by an object in a radiometer scene, the physical temperature of the object must be multiplied by its MMW emissivity. So we have for non-black bodies

$$B_e = \epsilon \frac{2kT}{\lambda^2} , \quad (2)$$

where B_e is the effective thermal source brightness and ϵ is the MMW emissivity of the object. This equation shows a linear relationship between the temperature of any object in the radiometer scene and the power that it emits. This makes it convenient to express the equations governing MMW radiometry in terms of temperature, as will be done in this report.

In order to analyze the passive MMW detection and imaging of a target embedded in a scene, the sources of radiation present are divided into four categories: emissions from the target, emissions and reflections from the scene surrounding the target, target reflections of sources inside or outside the scene, and emissions of the atmosphere within the field of view of the sensor [6]. The temperature present at the sensor antenna can be written as a sum of temperatures:

$$T_{\text{total}} = T_{\text{target}} + T_{\text{background}} + T_{\text{reflected}} + T_{\text{atmos}} , \quad (3)$$

where T_{total} is in Kelvin. The expression does not include the temperature added by the sensor, as will be discussed later. Following is a description of each of the terms in equation (3).

The temperature present at the antenna due to target emissions is proportional to the product of the target's physical temperature and its emissivity, and is written

$$T_{\text{target}} = \frac{\epsilon T \eta}{L_a}, \quad (4)$$

where η is the ratio of the target area to the entire area covered by the sensor antenna beam (fill factor), and L_a is the atmospheric absorption factor of the air between the target and the sensor. L_a is given by

$$L_a = 10^{[L_{\text{atm}} R / 10^4]}, \quad (5)$$

where L_{atm} is the atmospheric attenuation in decibels/kilometer and R is the distance from the sensor to the target in meters. L_{atm} often varies over the signal path between the scene and the sensor. In some cases, though, it can be considered constant with a reasonable degree of accuracy. The part of the scene temperature that is due to the background around the target within the sensor antenna beam is expressed as a sum of emissions from the background and reflections of sky radiation by the background, and is given by

$$T_{\text{background}} = \left(\frac{\epsilon_g T_g + (1 - \epsilon_g) T_{\text{sky}}}{L_a} \right) (1 - \eta), \quad (6)$$

where ϵ_g is the emissivity of the background, T_g is the physical temperature of the background, and T_{sky} is the noise equivalent sky temperature incident upon the target area. This value is given by the expression

$$T_{\text{sky}} \cong T_{\text{atm}} \left(1 - \frac{1}{L_z} \right) + \frac{T_{cb}}{L_z}, \quad (7)$$

where T_{atm} is the mean atmospheric temperature, usually taken to be 290 K; L_z is the total zenith absorption factor of the atmosphere above the target; and T_{cb} is the MMW cosmic background radiation temperature of 3 K. This expression approximates the contribution of the atmosphere and the cosmic background to the overall sky temperature by only considering contributions from the zenith. This is approximately correct over ± 70 degrees from the zenith, beyond which sky temperatures rapidly approach 290 K [7]. For cases such as the landing-aid scenario, where the background has a high reflectivity and is being viewed at a grazing angle, a new expression must be used.

The part of the measured scene due to reflections of T_{sky} by the target is given by

$$T_{\text{reflected}} = \frac{(1 - \varepsilon)T_{\text{sky}}\eta}{L_a} . \quad (8)$$

Again, I assume that most of the sky radiation that is reflected by the target and is incident upon the antenna is not from the horizon. The last source of MMW radiation that is incident upon the antenna is due to the emission of the atmosphere between the target and the sensor. This is expressed as

$$T_{\text{atmos}} = T_a \left(1 - \frac{1}{L_a}\right) , \quad (9)$$

where T_a is the ambient temperature. As can be seen, if the attenuation of the atmosphere is small, then its MMW radiation contribution goes to zero. These equations were used to calculate the theoretical scene temperatures incident upon the antenna of a radiometer, as is discussed in section 4. The values of MMW atmospheric attenuation and material emissivity are available from the literature for many atmospheric conditions and scene materials [7–12]. Section 4 gives a detailed description of the models used to calculate the theoretical scene temperatures.

A MMW radiometer, being an imperfect sensor, attenuates received signals and can have a large noise level compared to the radiation signal it receives. Because of this, an important performance parameter of any radiometer is the standard deviation of its noise, or minimum temperature resolution. This quantity is essentially a measure of the degree to which a system can detect small scene temperature changes and is expressed as [7]

$$\Delta T_{\text{min}} = \kappa \frac{FT_a}{\sqrt{B\tau}} . \quad (10)$$

In this expression, F is the cascaded receiver noise figure, B is the receiver's bandwidth, κ is a constant that depends on the type of radiometer used, and τ is the signal integration time. As can be seen, increasing the detection bandwidth or integration time and decreasing the noise figure can minimize ΔT_{min} and thereby improve system sensitivity.

Many radiometers produce a large noise signal at their output that is due to system noise. This signal can be represented by the quantity of system noise temperature, T_n , where $T_n = (F - 1)T_a$. This quantity can easily be 3000 K or higher. Detecting small changes (~ 1 K) in scene temperature on top of this large system noise signal requires that the noise level of the receiver be very stable over time. As a method to avoid this problem, it is common to build a noise subtraction device into a radiometer. Commonly, the device used is an RF switch that periodically switches the input of the sensor to a

reference noise source or load (Dicke switch radiometer) [13]. This reference signal level is subtracted from the scene signal during processing and removes system gain variations from the measurement. The duty cycle of this switch affects the value of κ in equation (10). A 50-percent duty cycle on the switch would make $\kappa = \sqrt{2}$.

3. Atmospheric Effects Theory

The scene temperatures measured with a passive MMW imager are strongly affected by atmospheric conditions. At MMW frequencies, the primary sources of attenuation in the atmosphere are water vapor and liquid water. The data presented later in this report are calculations based on the modeling of MMW atmospheric attenuation for varying amounts of water vapor, fog, clouds, and rain. The equations describing MMW attenuation for these conditions are well established and are presented below [14].

Attenuation due to water vapor in the air in units of decibels/kilometer is given by the expression

$$\alpha_v = cv\theta^y, \quad (11)$$

where v is the water vapor density of the air in g/m^3 , θ is defined as $300/T$, where T is the atmospheric temperature in Kelvin; and c and y are constants that depend on frequency. For frequencies near 94 GHz, $c = 0.049$ and $y = 2.4$. The expression assumes that the atmospheric pressure is constant at 101 kPa.

Attenuation due to fog is expressed in decibels/kilometer as

$$\alpha_f = bf\theta^y, \quad (12)$$

where f is the suspended liquid water content of the fog in g/m^3 and b and y are frequency-dependent constants of 3.45 and 3.6, respectively, for frequencies near 94 GHz. The attenuation due to clouds is given by the same equation since the attenuation phenomena are basically the same.

The attenuation of MMW radiation by rain is given in decibels/kilometer by the expression

$$\alpha_r = aR^x, \quad (13)$$

where R is the rain rate in millimeters per hour and a and x are frequency-dependent constants of 1.03 and 0.76, respectively, for frequencies near 94 GHz and rain rates less than 25 mm/hr.

Another atmospheric parameter that was required for the modeling was the clear air MMW zenith attenuation. In clear air, the theoretical value is an integral of the altitude-dependent attenuation from ground level up to several kilometers. The calculation is often performed by quantizing the atmosphere into altitude layers that each have specific attenuation characteristics (U.S. Standard Atmosphere). A sufficient quantity of theoretical zenith attenuation data was not found for this study, so measured zenith attenuation test data were used because of their availability [14]. Other sources of zenith attenuation, such as clouds and rain, were calculated and added to the clear air value to give the overall zenith attenuation value used for a given set of environmental conditions.

4. Results

The algorithm written to calculate radiometer performance incorporates the concepts and equations explained in the previous two sections. The focus of the algorithm was to simulate three scenarios that are considered to be possible Army applications of MMW radiometer technology. The three scenarios of interest are: a ground-based armored vehicle imager, an airborne imager of armored vehicles, and a passive landing system able to image concrete runways through fog. The modeling of the sensor required that assumptions be made about its antenna characteristics, and the algorithm results are therefore specific to those parameters. The variation of the results with different antenna parameters will be discussed in section 5. Emissivity and object sizes were considered when calculating scene temperatures. The results of these calculations are presented in graphs of ΔT versus range, where ΔT is the temperature difference between an image pixel (beam position) that is pointed at the target and an image pixel that is not. A comparison of this value to the minimum temperature resolution, ΔT_{\min} , of a radiometer indicates whether the sensor can detect the target in its field of view.

4.1 Armored Target Imaging

The armored target imaging scenarios (ground-based and air-based) present very similar modeling problems. Obviously, the principal similarity is that they both require calculating the MMW signal emissions and reflections of an armored target, although from different aspect angles. A metal target on the ground stands out in a MMW radiometer image because it has a low emissivity at MMW frequencies and therefore reflects the sky, which often has an emitted signal strength, or temperature, lower than the background temperature (nominally 290 K). So, a metal target's temperature primarily varies with sky temperature, as opposed to a highly emissive target, whose MMW temperature varies with its physical temperature. For this reason, armored targets often appear colder than their surroundings in a MMW radiometer image. How much colder the target appears depends on a

number of things. If there is a great deal of moisture in the air above the target or between the target and the sensor, the target temperature incident upon the antenna is higher than it would be in clear conditions due to the high MMW emissions of the moist air. The other main factor that affects a target's MMW temperature is the shape and orientation of its reflecting surfaces. A target usually reflects radiation from a variety of directions at various noise equivalent temperatures. The parts of the target that reflect the background or the horizon blend in with the background and effectively reduce the cross-sectional area of the target that can be detected with the sensor. Rather than ray trace all the MMW signals involved in each scenario to calculate a scene temperature, it is often simplest to estimate the percentage of the target surface area that is reflecting the cold sky (± 70 degrees from the zenith). This area can then be used to calculate the target fill factor for a given antenna beam position.

For the metal target scenarios considered here, it was assumed that the target was non-emissive (reflectivity = 1), 3 m wide by 3 m tall by 6 m long, and head-on to the sensor. The sensor was assumed to measure the scene from nadir angles (angle from the nadir) of 90 degrees and 30 degrees for the ground-to-ground and air-to-ground scenarios, respectively. For both views of the target, the cross-sectional target area was calculated. However, as stated earlier, only a fraction of this area reflects radiation from the cold sky. So, as an approximation, the target was assumed to be equivalent to a flat plate that reflects the cold sky radiation and is equal in size to 50 percent of its total cross-sectional area. The target areas used were 4.5 m² and 10 m² for the ground-to-ground and air-to-ground scenarios, respectively.

Scene temperatures were calculated for both metal target scenarios. These values resulted from calculations of target temperature, atmospheric attenuation, and atmospheric emission, all of which contribute to the final signal present at the sensor. The principal difference between the airborne sensor and the ground-based sensor calculations was that the signal propagating to the airborne sensor was affected by clouds and other altitude-related changes in attenuation along its path. In the ground-to-ground scenario, it was assumed that the attenuation coefficient remained constant on the path from the target to the sensor.

4.2 Landing System

The aircraft-landing-in-fog scenario presented other challenges. The modeling of a concrete runway surrounded by grass requires a more detailed representation of the electromagnetic properties of the materials involved. Each reflects and emits quantities of MMW radiation proportional to its reflectivity and emissivity, respectively. These quantities are dependent on polarization, aspect angle, and surface roughness. The runway can be considered smooth at MMW frequencies and can therefore be treated as a

specular reflector with a low emissivity. For this scenario, an aircraft approach angle of 4 degrees and a horizontal polarization is assumed. Horizontal polarization is chosen to enhance the contrast between the concrete and the grass [16]. The runway is assumed to be 33 m wide and 800 m long. The emissivity of the concrete runway is assumed to decrease as the cosine from the normal, resulting in the value 0.07. The grass, on the other hand, must be treated as a diffuse reflector with a relatively high emissivity. The small amount of radiation that it does reflect is treated as an average temperature of the entire sky (about 190 K for 500-m fog depth) [15]. For this scenario, it is assumed that the grass has an emissivity of 0.9. This is 0.04 less than the normal incidence emissivity. The temperature of the runway and the surrounding grass can be calculated independently, assuming that the reflectivity of the runway and grass are equal to 1 minus their emissivities. It becomes apparent that the runway primarily reflects the horizon, which has a temperature of about 290 K. What little radiation is due to emission is the result of an assumed 290 K physical temperature. Therefore the net MMW temperature of the runway is about 290 K. The grass can also be assumed to have a physical temperature of 290 K, but it has a finite reflectivity that reflects the average sky temperature. This results in the grass having a temperature that is colder than the runway. Taking the difference between the runway and grass temperatures and adjusting for atmospheric effects between the scene and the radiometer results in the temperature contrast of the scene present at the antenna.

The following pages present the calculated scene temperature results for various weather conditions. Ten different weather scenarios were modeled. They are: three different water vapor conditions with clear air, two fog types, two cloud cover types, and three rain conditions. The MMW attenuation coefficients were calculated using common scattering and absorption models for water vapor and droplets. The physical atmospheric temperature was assumed to be 17°C for all 10 conditions. The water vapor values used were 0.71, 7.15, and 14.3 g/m³. Two fog types were modeled: 100- and 24-m visibility. The fog was assumed to extend from the ground up to 500 m. The first cloud model was a cumulus congestus cloud extending from 1000 to 2000 m. The second was a stratus cloud extending from 1000 to 2000 m. The three rain rates used were 1, 5, and 10 mm/hr. Other atmospheric parameters are presented with the graphs.

Assumptions were made concerning the sensor antenna so that values of spatial resolution and beam fill factors could be determined. A 94-GHz, 3-by 3-ft square, fixed, planar antenna was used for these calculations. A beamwidth coefficient of 0.86 was assumed, which results in a beamwidth of 0.17 degrees at 94 GHz. This corresponds to the resolution possible with a uniform square aperture. Beyond this, no assumptions were made

concerning the sensor. Losses in the antenna itself were considered part of the receiver noise figure and not considered. The scene temperatures calculated are a representation of the signal present at the sensor before the antenna.

Figures 1 through 4 show the results of the ground-to-ground scenario scene-temperature calculations versus target-to-sensor range. As stated before, ΔT is the scene temperature of an image pixel filled by background minus the scene temperature of a pixel in which there is a target. The reference line on the graphs at $\Delta T = 4$ K represents an arbitrary minimum temperature resolution of a radiometer, although values at least an order of magnitude lower are attainable. The target size used for this scenario is 4.5 m^2 .

Note in figures 1 through 4 that, at ranges closer than 1000 m, there is an abrupt change in the slope of the curves. This is because at close ranges the antenna beam area is smaller than the target. When target range increases, this area becomes larger than the target and the beam fill factor dominates the shape of the curve. Also note that temperature contrast is degraded most significantly by thick fog, cumulus congestus clouds, and rain (fig. 2 to 4). Cumulus congestus clouds affect scene contrast by increasing the amount of the downwelling sky radiation as opposed to fog and rain, which degrade the scene through signal attenuation on the path from the scene to the sensor.

Figure 1. Calculated radiometer scene contrast, $\Delta T(\text{K})$, for ground-to-ground scenario in clear air with various water vapor densities.

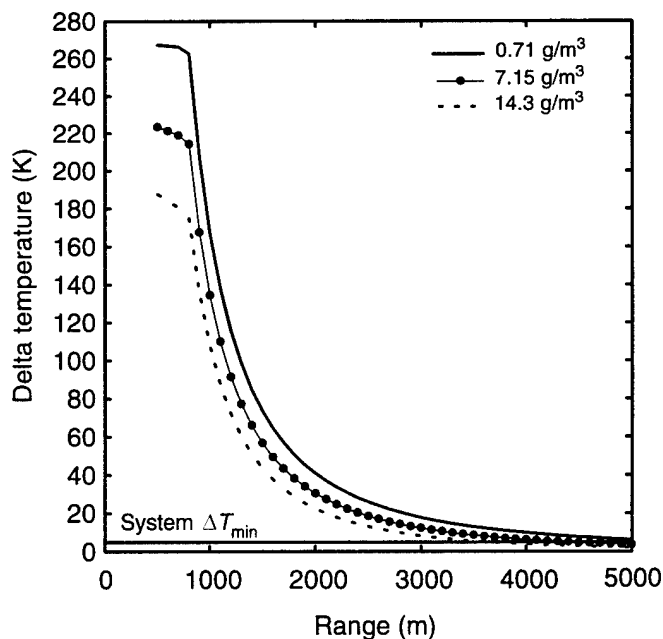


Figure 2. Calculated radiometer scene contrast, $\Delta T(K)$, for ground-to-ground scenario through two fog visibilities (500-m fog depth).

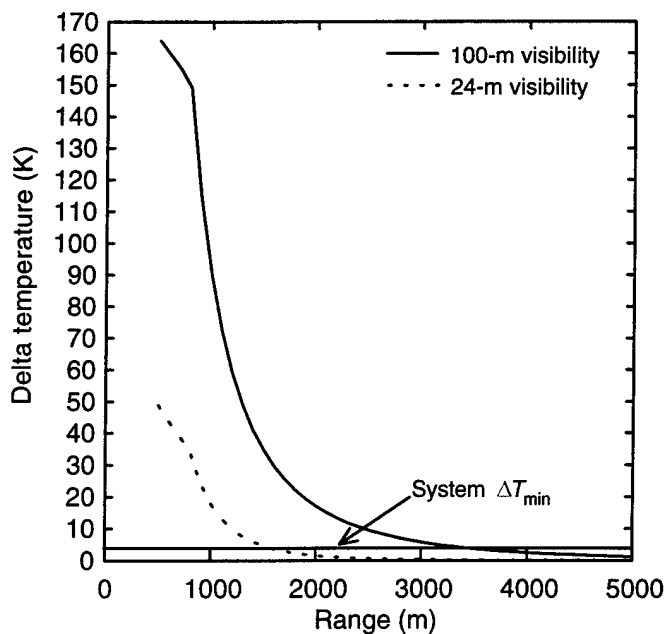


Figure 3. Calculated radiometer scene contrast, $\Delta T(K)$, for ground-to-ground scenario for two cloud cover types (clouds from 1000 to 2000 m).

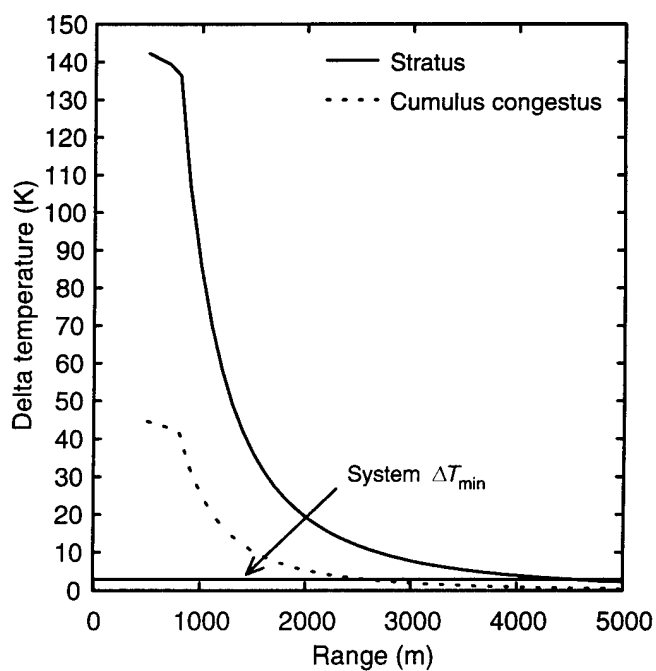
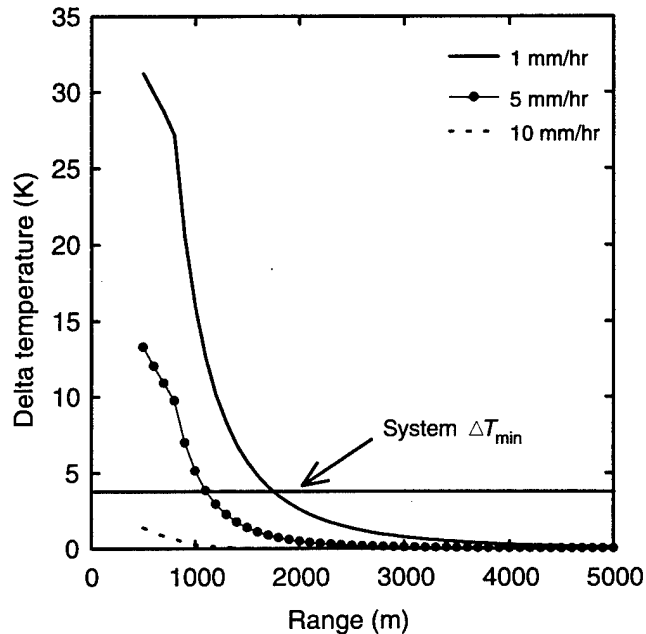


Figure 4. Calculated radiometer scene contrast, $\Delta T(K)$, for ground-to-ground scenario in various rain rate conditions.



The graphs show that detection ranges vary a great deal with changes in environmental conditions. For the purposes of discussion, I define the range at which the signal-to-noise ratio (S/N) equals 1 to be a figure of merit referred to as the noise cutoff (NC) range. Figure 1, which includes the 0.71 g/m^3 water vapor situation, shows an NC range of greater than 5 km for a sensor with a minimum temperature resolution of 4 K. Figure 4 shows that in heavy rain the same sensor would have an NC range of less than 500 m. A system with a ΔT_{min} of a few tenths Kelvin would be required to achieve an NC range of 1 km in heavy rain (not considering background clutter).

Figures 5 through 8 show scene temperature contrast in the air-to-ground scenario under the same environmental conditions as figures 1 through 4. The scene contrast values for this scenario were calculated using a 10-m^2 target. The target size is larger than in the ground-to-ground scenario because the airborne sensor views more of the target surface area. Also note that there are occasionally two abrupt slope changes in this set of graphs (i.e., fig. 7). This is due to the beam-fill-factor effect described earlier, as well as attenuation that changes with range as the signal from the target scene passes through varying layers of clouds, fog, and rain. Overall, the air-to-ground scene temperature contrasts are equal to or better than the ground-to-ground case, with the exception of the rain conditions. Performance is better because the fill factor is larger for this scenario. This scenario is worse, though, for heavy rain situations, where the signal path runs through both the rain and cloud deck on its way to the sensor.

The calculated results of the landing-aid scenario are shown in figure 9. Only the fog scenario was considered for this case. The shapes of the curves are quite a bit different from the metal target scenarios. This is largely because, even at 5 km, the runway is large compared to the pixel size, or

Figure 5.
Calculated
radiometer scene
contrast, $\Delta T(K)$, for
air-to-ground
scenario in clear air
with various water
vapor densities.

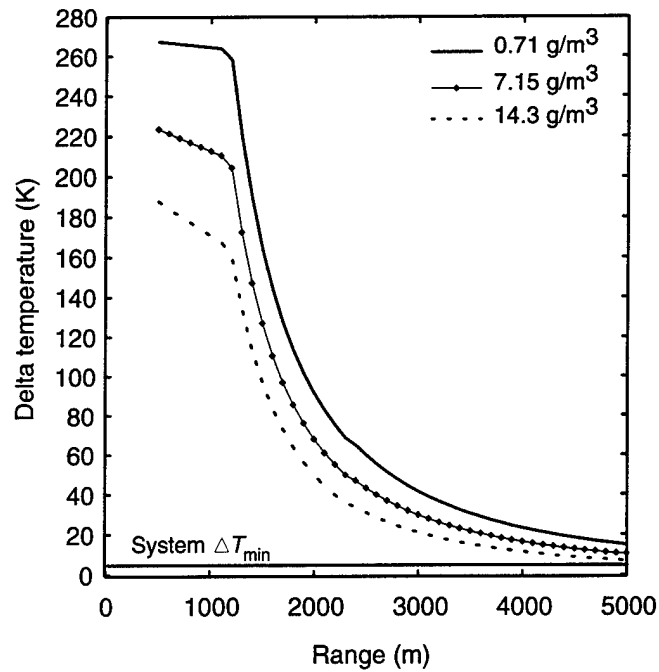


Figure 6. Calculated
radiometer scene
contrast, $\Delta T(K)$, for
air-to-ground scenario
through two fog
visibilities (500-m fog
depth).

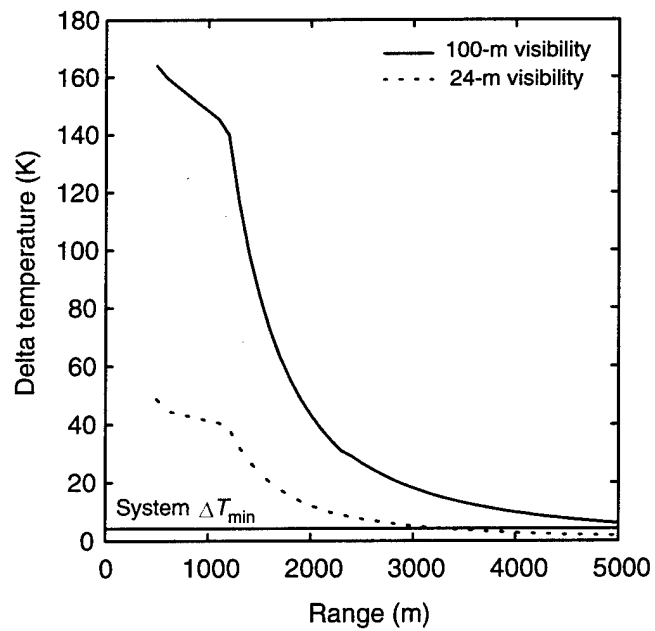


Figure 7. Calculated radiometer scene contrast, $\Delta T(K)$, for air-to-ground scenario for two cloud cover types (clouds from 1000 to 2000 m).

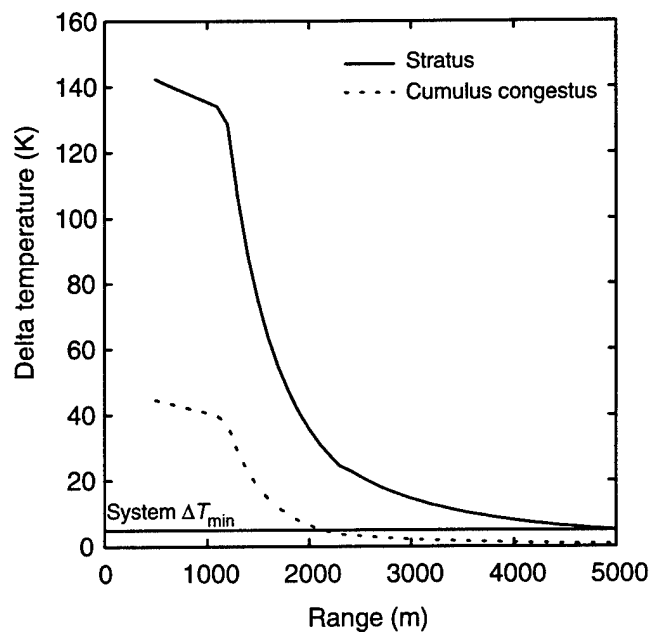


Figure 8. Calculated radiometer scene contrast, $\Delta T(K)$, for air-to-ground scenario in various rain rate conditions.

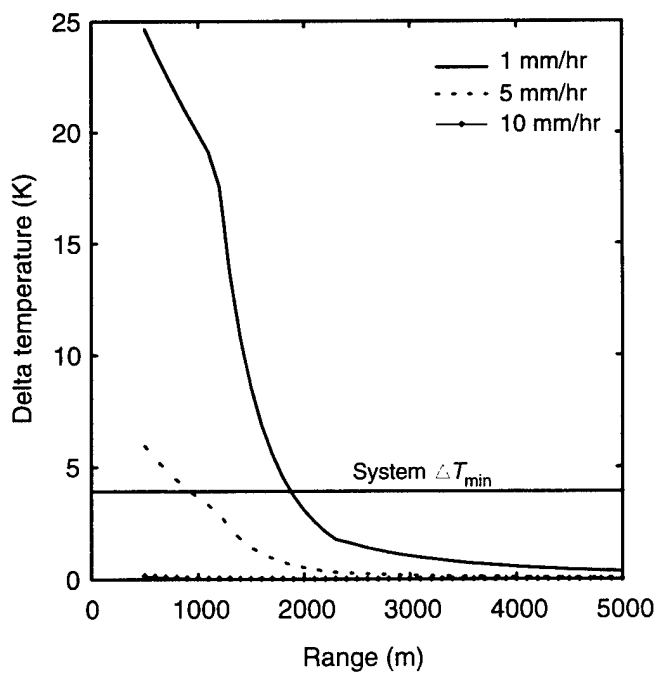
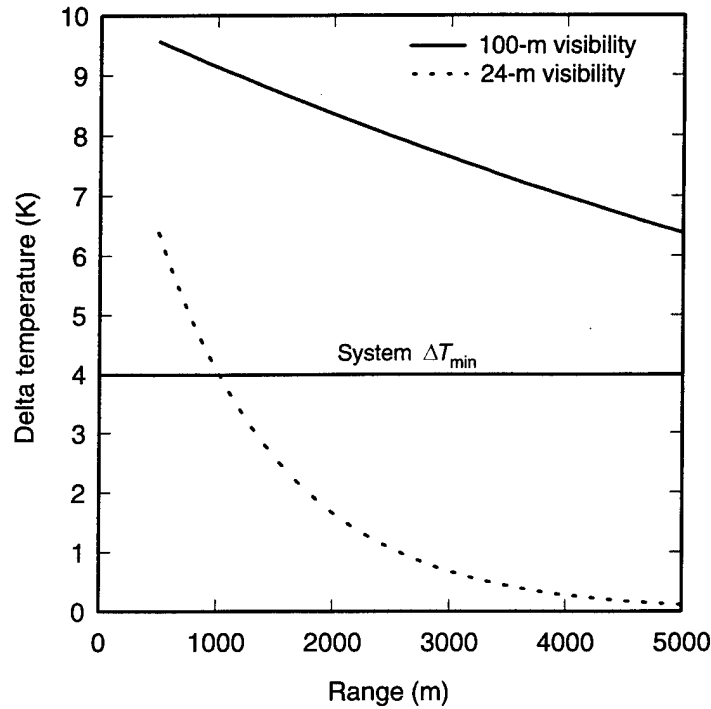


Figure 9. Calculated radiometer scene contrast, $\Delta T(K)$, for landing-aid scenario through two fog visibilities (500-m fog depth).



beamwidth, of the radiometer antenna. At an approach angle of 4 degrees, the runway appears 33 m wide by 56 m tall, and at a range of 5 km the antenna pixel size is about 15 by 15 m. Therefore, from 500 m to 5 km, the runway is always bigger than the image pixel. The 24-m fog shows a quicker drop in scene contrast than the 100-m fog, as is expected.

5. Discussion

The graphs presented in the previous section show the scene temperature contrast present at the sensor antenna (ΔT) for three imaging scenarios in a variety of environmental conditions. Given a sensor with some minimum temperature resolution, ΔT_{\min} , the results indicate the NC ranges for the target scene. Tables 1 through 3 summarize these results in terms of noise cutoff ranges for each of the scenarios for systems with temperature resolutions of 2, 4, and 10 K. The discussion that follows refers to the 4 K system. The 2 and 10 K systems are presented for comparison. Radiometers with temperature resolutions much lower than 2 K have been demonstrated, but higher values were chosen for this study since these values are easily realized.

Tables 1 through 3 show that the maximum NC range increases as system temperature resolution improves. They also show that steady-to-heavy rain and dense fog have the worst effect on MMW radiometer performance. In the ground-to-ground scenario (table 1), the sensor with a ΔT_{\min} of 4 K has an NC range greater than 2 km, except in drizzle/rain conditions and the heavy fog condition. By comparison, the heavy fog does not have as severe

Table 1. Noise cutoff ranges for ground-to-ground metal target scenario for various environmental conditions and temperature resolutions. Ambient temperature = 17°C.

Environmental condition	Noise cutoff range (km) for given ΔT_{\min}		
	2 K	4 K	10 K
5% relative humidity, clear air	>5.0	>5.0	3.9
50% relative humidity, clear air	>5.0	4.7	3.2
100% relative humidity, clear air	5.0	3.9	2.7
100-m visibility fog	4.2	3.4	2.4
24-m visibility fog	1.8	1.5	1.2
Stratus clouds 1000 to 2000 m	>5.0	3.9	2.6
Cumulus congestus clouds 1000 to 2000 m	2.9	2.2	1.5
Drizzle, 1 mm/hr, cumulus congestus	2.1	1.7	1.2
Steady rain, 5 mm/hr, cumulus congestus	1.3	1.0	0.7
Heavy rain, 10 mm/hr, cumulus congestus	<0.5	<0.5	<0.5

Table 2. Noise cutoff ranges for air-to-ground metal target scenario for various environmental conditions and temperature resolutions. Ambient temperature = 17°C.

Environmental condition	Noise cutoff range (km) for given ΔT_{\min}		
	2 K	4 K	10 K
5% relative humidity, clear air	>5.0	>5.0	>5.0
50% relative humidity, clear air	>5.0	>5.0	5.0
100% relative humidity, clear air	>5.0	>5.0	4.2
100-m visibility fog	>5.0	>5.0	3.9
24-m visibility fog	4.6	3.3	2.1
Stratus clouds 1000 to 2000 m	>5.0	>5.0	3.5
Cumulus congestus clouds 1000 to 2000 m	3.1	2.2	1.7
Drizzle, 1 mm/hr, cumulus congestus	2.2	1.8	1.4
Steady rain, 5 mm/hr, cumulus congestus	1.3	0.8	<0.5
Heavy rain, 10 mm/hr, cumulus congestus	<0.5	<0.5	<0.5

Table 3. Noise cutoff ranges for landing-aid scenario for various environmental conditions and temperature resolutions. Ambient temperature = 17°C.

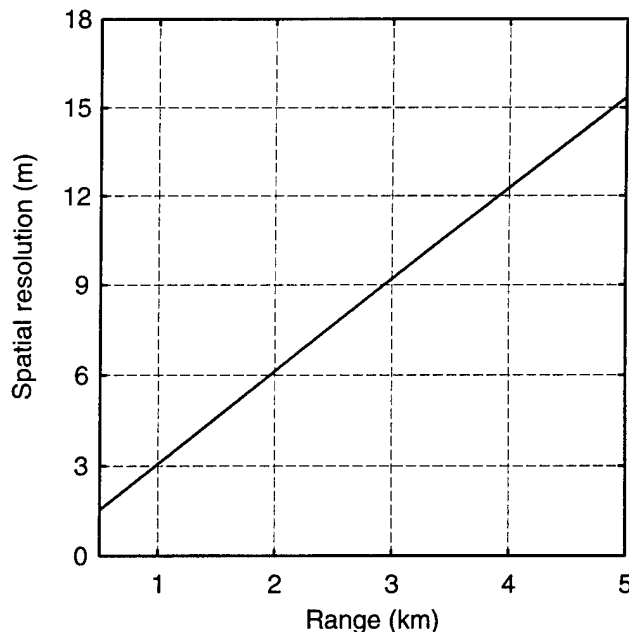
Environmental condition	Noise cutoff range (km) for given ΔT_{\min}		
	2 K	4 K	10 K
100-m visibility fog	>5.0	>5.0	>5.0
24-m visibility fog	1.8	1.1	<0.2

an effect in the air-to-ground scenario (table 2). This is because, as range increases the sensor emerges from the fog bank and therefore does not experience fog attenuation over the full path length to the target. Also note the decrease in NC range that results from cloud cover in the metal target scenarios.

One limitation of these results, however, is that clutter has not been considered. There will undoubtedly be objects in the scene (metal, concrete, water, etc.) that are not the target of interest. These objects could affect the temperature of an image pixel enough to generate significant false alarms. In addition, background that is otherwise thought to be uniform could have a MMW temperature variation of up to 3 K [6]. To effectively determine what in the scene is a target and what is clutter, the sensor has to image, or spatially resolve, the target as well as detect it. Resolving a target (determining its approximate size) requires that the sensor's beamwidth be, at most, half the size of the target, as described by the Rayleigh criteria. Figure 10 presents the spatial resolution or pixel size of the 95-GHz, 3- by 3-ft square antenna that was used in the scene temperature calculations as a function of range.

The graph shows that, for the head-on metal target (3 m wide by 3 m tall), the target is two pixels wide at about 500 m. A broadside metal target 6 m long would have about two pixels on target at a range of 1 km. Obviously, with an antenna of this size, tank-type targets could not be resolved to allow recognition at ranges greater than 1 km, despite the fact that detection ($S/N = 8$ dB) is possible at larger ranges in a variety of environmental conditions. This limits this type of sensor to applications involving close-range, foul-weather imaging, or cueing of higher resolution sensors.

Figure 10. Spatial resolution of 3- by 3-ft square antenna at 94 GHz. Beamwidth constant 0.86.



The landing-aid scenario, however, does not have this problem. The runway fills two pixels out past 4 km with a 3- by 3-ft square antenna so resolution is not an issue. However, scene contrast is not that high (fig. 9). Detection ($S/N = 8$ dB) at 1 km of a concrete runway in a dense fog would require a sensor with a temperature resolution of 0.6 K or better.

These results allow us to draw conclusions concerning the potential performance of this type of sensor for the three scenarios considered. The results from the air-to-ground metal target scenario indicate that, under certain conditions, this sensor has the spatial resolution and S/N required to image metal targets. If ranges do not exceed 1 km, then the system's spatial resolution is sufficient to image individual tank-sized targets. Beyond 1 km, the system may be able to detect targets, but not determine target sizes. Larger targets or groups of targets could be imaged and recognized at greater ranges. At 1 km, the sensor shows good performance in all the environmental conditions considered, except heavy rain. As shown in table 2, the noise cutoff range in thick cumulus clouds extends to 2.2 km with a 4-K system noise temperature. Therefore, one application of this sensor is the detection or imaging of tank-sized metal ground targets from an altitude of 1 km in the clouds or above a fog bank. The cloud/fog cover takes full advantage of the covert nature of the sensor, while still allowing target imaging or detection. The sensor could be used at greater ranges to detect larger targets or target configurations that may allow a degree of recognition. Using the sensor in clear air would not be useful because of the sufficient quality of IR and video sensors under these conditions.

In the landing-aid scenario, the scene contrast is marginal in both fog conditions because of the assumed system thermal sensitivity of 4 K. A system with a 0.6-K thermal sensitivity, however, could be used for imaging in this scenario. Even in dense fog, the results show that detection of a runway would be possible at 1 km. At this range the runway is five image pixels wide, so good target resolution is also possible. Detecting unimproved dirt or grass runways would probably only be practical if active or passive beacons are used.

The ground-to-ground scenario presents the poorest performance of the three scenarios. This is because the target is smaller and therefore resolved only at closer ranges. The range required for imaging a 6-m-wide target (broadside tank) with a 3- by 3-ft square antenna is 1000 m. Given this and the results from table 1, the best applications for the ground-based imager would be those that require it to image individual targets at ranges of 500 to 1000 m in fog. Under these conditions, the sensor is limited not by the fog, but by the imager's spatial resolution. As in the air-to-ground scenario, operation at longer ranges would be possible if only target detection is required. However, the sensor could image larger targets, such as installations or groups of vehicles, from ranges greater than 1 km. In atmospheric conditions other than fog, a ground-based passive MMW sensor would have no advantage over other passive sensors with better spatial resolution.

6. Conclusion

This report presents scene temperature calculations for a 94-GHz passive MMW imager in ten different environmental conditions and for three target scenarios of interest to the Army. This study was conducted to determine the environmental conditions under which passive imaging quality degrades. In the case of armored vehicle imaging, it was found that, for a 3-by 3-ft square, 94-GHz, fixed antenna, spatial resolution limits image quality before most environmental conditions do. In the ground-to-ground scenario, resolution of a tank-sized target occurs between 500 and 1000 m, where only 10-mm/hr rain limits the sensor's noise cutoff range. In the air-to-ground scenario, the resolution range is about 1 km where, again, only rain limits the image quality further. Such a sensor, used to image tank-sized targets, would be restricted to use at close range and in foggy (ground-based or airborne) or cloudy (airborne only) weather, where other types of passive sensors fail. Detection of large targets or arrays of targets is possible at greater ranges, however. In addition, the landing-aid scenario has been shown to be a potentially good application for a passive MMW sensor, given a sufficient system thermal resolution.

Acknowledgments

I would like to thank Dr. Joseph Nemarich for his editorial work on this report, as well as for many useful conversations related to passive imagers. In addition, I would like to thank Mr. Bruce Wallace for his advice and comments during the editing of this report.

References

1. Young, S. K., R. A. Davidheiser, B. Hauss, P. S. Lee, M. Mussetto, M. M. Shoucri, and L. Yujiri, *Passive Millimeter Wave Imaging Systems for Military Missions—Time for a Revisit*, NATO Workshop on Military Application of Millimeter Wave Imaging, Hanscom AFB (November 1992).
2. Appleby, R., and A. H. Lettington, *Passive Millimetre Wave Imaging*, IEEE Electronics and Communications Engineering Journal, pp. 13–16 (February 1991).
3. Suess, H., K. Gruner, and W. Wilson, *Passive Millimeter-Wave Imaging—A Tool for Remote Sensing*, Alta Frequenza, Vol. LVIII—N 5–6, pp. 457–465 (September–December 1989).
4. Swift, C., D. LeVine, and C. Ruf, *Aperture Synthesis Concepts in Microwave Remote Sensing of the Earth*, IEEE Transactions on Microwave Theory and Techniques, Vol. 39, No. 12, pp. 1931–1935 (December 1991).
5. Lovberg, J. A., R. C. Chou, and C. Martin, *Real-Time Millimeter-Wave Imaging Radiometer for Avionic Synthetic Vision*, SPIE Proceedings, Vol. 2220, Sensing, Imaging, and Vision for Control and Guidance of Aerospace Vehicles (April 1994).

6. Wilson, W. J., R. J. Howard, A. C. Ibbott, G. S. Parks, and W. B. Ricketts, *Millimeter-Wave Imaging Sensor*, IEEE Transactions on Microwave Theory and Techniques, Vol. MTT-34, pp. 1026-1035 (October 1986).
7. Galliano, J. A., "MMW Radiometry," Chapter 18 of *Principles and Applications of Millimeter-Wave Radar*, edited by N. C. Currie and C. E. Brown, Artech House, Norwood, MA (1987).
8. Mundie, L. G., *Passive Millimeter-Wave Radiometry and Some Possible Applications*, Rand Corporation, R-1175-ARPA (April 1973).
9. Bogush, A. J., *Radar and the Atmosphere*, Artech House, Norwood, MA (1989).
10. Preissner, J., *The Influence of the Atmosphere on Passive Radiometric Measurements*, AGARD Conference Proceedings No. 245, Millimeter and Submillimeter Wave Propagation and Circuits, pp. 43-1 to 48-14 (4-8 September 1978).
11. Ulaby, F. T., R. K. Moore, and A. K. Fung, *Microwave Remote Sensing: Active and Passive*, Vols. I, II, and III, Artech House, Norwood, MA (1986).
12. Ulaby, F. T., A. K. Fung, and S. Wu, *The Apparent Temperature and Emissivity of Natural Surfaces at Microwave Frequencies*, University of Kansas, 133-12, THEMIS Contract DAAK02-68-C-0089 (March 1970).
13. Dicke, R. H., *The Measurement of Thermal Radiation at Microwave Frequencies*, The Review of Scientific Instruments, Vol. 17, No. 7, pp. 268-275 (July 1946).
14. Liebe, H. J., *Atmospheric EHF Window Transparencies Near 35, 90, 140, and 220 GHz*, IEEE Transactions on Antennas and Propagation, Vol. AP-31, pp. 127-135. (January 1983).
15. King, D. D., "Passive Detection," Chapter 39 of the *Radar Handbook*, edited by M. I. Skolnik, McGraw-Hill Book Company, New York (1970).
16. Hollinger, J. P., and L. A. Rose, *37 GHz Radiometric Background Measurements*, Naval Research Laboratory report for the U.S. Army Armament Research and Development Center (5 June 1990).

Distribution

Admnstr
Defns Techl Info Ctr
Attn DTIC-OCP
8725 John J Kingman Rd Ste 0944
FT Belvoir VA 22060-6218

Under Secy of Defns for Rsrch & Engrg
Attn Rsrch & Advncd Techlgy
Depart of Defns
Washington DC 20310

CECOM NVESD
Attn AMSEL-RD-NV-ASD M Kelley
Attn AMSEL-RD-NV-TISD F Petito
Attn Techl Lib
FT Belvoir VA 22060

DARPA
Attn TTO M McHenry
Attn ISO T Lawrence
Attn ETO L Sobolewski
3701 N Fairfax Dr
Arlington VA 22203-1714

Dpty Assist Scy for Rsrch & Techl
Attn SARD-TT F Milton Rm 3E479
Attn SARD-TT D Chait
Attn SARD-TT C Nash Rm 3E479
The Pentagon
Washington DC 20310-0103

Hdqtrs Dept of the Army
Attn DAMO-FDQ MAJ M McGonagle
400 Army Pentagon
Washington DC 20310-0460

Nav Rsrch Lab
Attn 2600 Techl Info Div
Attn 7223 G Poe
Attn 7223 S Highley
Attn 4555 W Waters
4555 Overlook Ave SW
Washington DC 20375

Nav Weapons Ctr
Attn 472310 D S Rogala
China Lake CA 93555

US Army Aberdeen Proving Ground
Attn AMXSY-MP
Aberdeen Proving Ground MD 21005

US Army Armament RDE Ctr
Attn SMCAR-FSP-A1 M Rosenbluth
Attn SMCAR-FSP-A1 R Collett
Picatinny Arsenal NJ 07806-5000

US Army CECOM NVESD
Attn AMSEL-RD-NV-RSPO A Tarbell
Mailstop 1112
FT Monmouth NJ 07703-5000

US Army Materiel Command
Attn AMCDM Dir for Plans & Analysis
5002 Eisenhower Ave
Alexandria VA 22333-0001

US Army Missile Lab
Attn AMSMI-RD Advanced Sensors Dir
Attn AMSMI-RD Sys Simulation & Dev Dir
Attn AMSMI-RD-AS-MM G Emmons
Attn AMSMI-RD-AS-MM M Christian
Attn AMSMI-RD-AS-MM M Mullins
Attn AMSMI-RD-AS-RPR Redstone Sci Info
Ctr
Attn AMSMI-RD-AS-RPT Techl Info Div
Redstone Arsenal AL 35809

US Army Rsrch Ofc
Attn B D Guenther
Attn C Church
PO Box 12211
Research Triangle Park NC 27709-2211

US Army Test & Evaluation Cmnd
Attn STEWS-TE-AF F Moreno
Attn STEWS-TE-LG S Dickerson
White Sands Missile Range NM 88002

Distribution (cont'd)

USA CRREL
Attn G D Ashton
72 Lyme Rd
Hanover NH 03755

USATEC
Attn J N Rinker
Attn P Johnson
7701 Telegraph Rd
Alexandria VA 22315-3864

Nav Surface Weapons Ctr
Attn DX-21 Library Div
Dahlgren VA 22448

Nav Weapons Ctr
Attn 38 Rsrch Dept
Attn 381 Physics Div
China Lake CA 93555

USAF Wright Lab
Attn WL/MMGS B Sundstrum
Attn WL/MMGS R Smith
101 W. Eglin Blvd Ste 287A
Eglin AFB FL 32542-6810

NASA Goddard Space Flight Ctr
Attn J Wang
Attn P Racette
Attn D M Le Vine
Greenbelt MD 20771

NASA Langley Rsrch Ctr
Attn B Kendall
Mail Stop 490
Hampton VA 23681-0001

Sandia Natl Lab
PO Box 5800
Albuquerque NM 87185

Georgia Institute of Technology
Georgia Tech Rsrch Inst
Attn Radar & Instrmntn Lab R McMillan
Attn Radar & Instrmntn Lab T L Lane
Atlanta GA 30332

Univ of Massachusetts at Amherst
College of Engineering
Attn C Swift
Amherst MA 01003

Aerojet
Attn YU C Ngan
1100 W Hollyvale Stret Bldg 1
Azusa CA 91702

Eviron Rsrch Inst of MI
Attn IRIA Lib
PO Box 134001
Ann Arbor MI 48113-4001

Gleason Research Associates
Attn T Gleason
5537 Twin Knolls Rd Ste 439
Columbia MD 21045-3272

Lockheed Martin Corp
Elect & Missile Div
Attn E Weatherwax
5600 Sand Lake Rd Mail Stop 450
Orlando FL 32819

Millitech Corp
Attn R Huegenin
S Deerfield Rsrch Park PO Box 109
S Deerfield MI 01373

Thermo Trex Corp
Attn J Galliano
Attn J Lovberg
10455 Pacific Center Court
San Diego CA 92121

TRW Space & Technology Div
Attn P Moffa
Attn M Shoucri
One Space Park
Redondo Beach CA 90278

US Army Rsrch Lab
Attn AMSRL-P-S-E B Perlman
Attn AMSRL-P-S-E M Cummings
FT Monmouth NJ 07703-5601

Distribution (cont'd)

US Army Rsrch Lab
Attn AMSRL-WT-WB R A McGee
Aberdeen Proving Ground MD 21005

US Army Rsrch Lab
Attn AMSRL-SE H Pollehn
10235 Burbeck Rd Ste 110
FT Belvoir VA 22060-5838

US Army Rsrch Lab
Attn AMSRL-CS-AL-TA Mail & Records
Mgmt
Attn AMSRL-CI-LLTech Lib (3 copies)
Attn AMSRL-CS-AL-TP Tech Pub (5 copies)
Attn AMSRL-SE J M Miller
Attn AMSRL-SE J Sichina

US Army Rsrch Lab (cont'd)
Attn AMSRL-SE-E J Pellegrino
Attn AMSRL-SE-EP Z G Sztankay
Attn AMSRL-SE-R A Sindoris
Attn AMSRL-SE-R E Burke
Attn AMSRL-SE-RI D Rodkey
Attn AMSRL-SE-RM B Wallace
Attn AMSRL-SE-RM D Wikner (20 copies)
Attn AMSRL-SE-RM H Dropkin
Attn AMSRL-SE-RM J Nemarich
Attn AMSRL-SE-RM J Silverstein
Attn AMSRL-SE-RM R Dahlstrom
Attn AMSRL-SE-RM R Wellman
Attn AMSRL-SE-RS T Kipp
Adelphi MD 20783-1197